Chemical Engineering Journal 453 (2023) 139781

Contents lists available at ScienceDirect

Chemical Engineering Journal

journal homepage: www.elsevier.com/locate/cej

Interfacing CrOx and CuS for synergistically enhanced water oxidation catalysis

Tofik Ahmed Shifa [a,*], Alessandro Gradone [b], Khabib Yusupov [c], Kassa Belay Ibrahim [a], Matteo Jugovac [d], Polina Makarovna Sheverdyaeva [e], Johanna Rosen [c], Vittorio Morandi [b], Paolo Moras [e], Alberto Vomiero [a,f,*]

[a] Department of Molecular Sciences and Nanosystems, Ca' Foscari University of Venice, Via Torino 155, 30170 Venezia Mestre, Italy
[b] Istituto per la microelettronica e i microsistemi (IMM), Consiglio Nazionale delle Ricerche (CNR), 40129 Bologna, Italy
[c] Materials Design, Department of Physics, Chemistry and Biology (IFM), Linköping University, 581 83 Linköping, Sweden
[d] Elettra Sincrotrone Trieste SCpA in Area Science Park, Campus di Basovizza S.S. 14 Km 163.5, I-34149 Trieste, Italy
[e] Istituto di Struttura della Materia-CNR (ISM-CNR), SS 14, Km 163.5, 34149 Trieste, Italy
[f] Division of Materials Science, Department of Engineering Sciences and Mathematics, Luleå University of Technology, SE-97187 Luleå, Sweden

ARTICLE INFO

Keywords:
Heterostructure
Chemical vapor deposition
Hydrothermal
Oxygen evolution
DFT

ABSTRACT

The sluggish kinetics associated with the oxygen evolution reaction (OER) limits the sustainability of fuel production and chemical synthesis. Developing catalysts based on Earth abundant elements with a reasonable strategy could solve the challenge. Here, we present a heterostructure built from CrOx and CuS whose interface gives rise to the advent of new functionalities in catalytic activity. Using X-ray photoelectron and absorption spectroscopies, we identified the multiple oxidation states and low coordination number of Cr metal in CrOx-CuS heterostructure. Benefitting from these features, CrOx-CuS generates oxygen gas through water splitting with a low over potential of 190 mV vs RHE at a current density of 10 mA cm^{-2}. The catalyst shows no evident deactivation after a 36-hours operation in alkaline medium. The high catalytic activity, inspired by first principles calculations, and long-time durability make it one of the most effective OER electrocatalysts.

1. Introduction

The oxygen evolution reaction (OER) is a pivotal route and often regarded as a bottleneck step in various processes of clean energy conversion and fuel transformations such as water splitting, [1] rechargeable metal-air batteries [2,3] and electrochemical synthesizers [4,5]. Lowering the overpotentials for OER contributes to lowering the cost of producing synthetic fuels. Currently, rutile-structured ruthenium (Ru) and iridium (Ir) oxides are the two best catalysts for OER. Yet, the large-scale application of these materials is limited by their low abundance and high price [6]. So far, various catalysts have been investigated based on Earth abundant elements of oxides, hydroxides, phosphides, nitrides and chalcogenides to respond to this existing challenge. The correlation between the electronic structure of transition metal oxides and their activities is crucial for understanding the design of efficient materials [7–13]. This has revealed important OER descriptors such as the number of d-electrons [14], eg orbital filling [15], bond covalency in metal–oxygen framework [16], and etcetera; with which the catalytic properties of transition metal oxides can be probed. Especially, transition metal eg filling is an interesting phenomenon in chromium-based catalysts that has recently won copious attention [17–21] due to the fact that Cr^{3+} cations exhibit a special electronic configuration ($t_{2g}^3e_g^0$) [22,23]. This type of electron configuration is favorable for conductivity, charge transfer and electron capture. A recent study shows that Cr plays a critical role in tuning the electronic structure of RuO_2 phase thereby delivering active and stable $Cr_{0.6}Ru_{0.4}O_2$ catalyst [24].

On the other hand, CuS has been proved to assist accelerated charge transfer when loaded on the surface of known catalysts such as TiO_2 [25–27] and MoS_2 [28]. It possesses a layered crystal structure with weak van der Waals interactions between individual planar Cu_2S_2 double layers [29,30]. Owing to this particular feature, it can offer a permeable channel for ion adsorption and transport. Moreover, CuS has a strong tendency to capture electrons and trigger electron transfer phenomena during catalysis. The design of nanocomposites with

* Corresponding authors.
E-mail addresses: tofikahmed.shifa@unive.it (T.A. Shifa), alberto.vomiero@unive.it (A. Vomiero).

https://doi.org/10.1016/j.cej.2022.139781
Received 16 August 2022; Received in revised form 1 October 2022; Accepted 10 October 2022
Available online 15 October 2022

atomically coupled dense heterointerfaces is a promising strategy to enhance performance [31–34]. Most recently, strong attention has focused on the development of metal oxide-sulfide interfaces for improved activity [35]. Metal sulfides, brought to metal oxides, are acknowledged for their intrinsically enhanced electrical conductivity and novel surface configuration. Especially, in OER catalysis, the formation of –OOH intermediates from the coordinated OH can be stimulated by the delocalized electrons among the attached oxygen, metal center, and the electronegative S atom [36]. It is, therefore, reasonable to design heterostructure between Cr_2O_3 and CuS which combines the advantageous features of both individual components and boost the catalysis in OER. In its general term, the combination between Cr-based and Cu-based catalysts exhibited promising activities in various applications [37–40]. Particularly, they demonstrated near those of precious metal-based catalysts in auto-emission control. This combination even surpasses various other catalysts in the order of $CuCr_2O_4 > Co_3O_4 > Fe_2O_3 > MnO > NiO > Cr_2O_3 > V_2O_5$ toward CO oxidation [41]. Herein, we present the rational design of a heterostructure between CrOx and CuS, hypothesizing that the interface could bring about atom-deficient/more active environment to trigger the adsorption and desorption of oxide moieties to eventually produce O_2 gas via water splitting. The design was first evaluated through theoretical calculations *via* VASP package. The results show a spontaneous decomposition of some of the molecules during OER process at the interaction of slabs, indicating less demanding overpotential for the process to flow. We also demonstrate the change in the atomic environment near the metal atoms before and after the formation of the heterointerface; and hence correlate their effect in enhancing the charge transfer phenomena during OER catalysis. The resulting electro-catalyst exhibits an overpotential of 190 mV vs RHE at 10 mA/cm^2, a small Tafel slope (57mVdec^{-1}) and stable chronopotentiometric performance under 10 mA cm^{-2}, 30 mA cm^{-2} and 100 mA cm^{-2} in 1 M KOH solution for 36 hr.

2. Experimental section

2.1. Theoretical Simulations:

First, we computationally studied if it is reasonable to interface Cr_2O_3 with CuS in terms of enhancing the OER activity. To this end, density functional theory (DFT) calculations were implemented via the Vienna ab initio simulation (VASP) package, being used to predict the ground state properties of a CuS surface and a Cr_2O_3/CuS interface, i.e. a Cr_2O_3 slab with an added CuS layer [42]. The projector-augmented wave (PAW) method [43] was used together with a kinetic energy cut-off of 520 eV, and the Perdew-Burke-Ernzerhow (PBE) functional was used to describe exchange–correlation effects. A three-layered CuS (1 0 0) supercell slab with 54 Cu and 54 S atoms was modelled to approximate the CuS surface. The bottom CuS layers were fixed at their bulk positions and the top layer was allowed to move during structural optimization. A similar procedure was done with the joint system, where the Cr_2O_3 (0 1 2) with 160 Cr and 240 O atoms were considered as the bottom part of the two-slab system, and CuS with 12 Cu and 12 S atoms was placed on top. The bottom layers of Cr_2O_3 were fixed at the bulk positions. The smaller thickness of the CuS layer in the joint system was chosen to reduce the computational cost. A schematic representation of the calculated slabs is represented in Fig. 1a and b. The k-point mesh was sampled using Gamma-centered grids of $2 \times 3 \times 1$, and $1 \times 3 \times 1$ for CuS, and Cr_2O3/CuS supercells, respectively. To account for the Van der Waals interaction a Van der Waals correction optB86b-vdW term was used [44]. Furthermore, the vacuum separation was kept to 15 Å. All structures were relaxed to a relative total energy less than 1×10^{-6} eV and overall cell pressure of less than 0.2 kBar.

For the OER calculations, the reactants/intermidiates (H_2O, OOH, OH, O_2, O) were placed separately on the slabs. For the CuS slab, the reactants were relaxed on top of the structure, whereas for the Cr_2O3/CuS slab, the molecules were placed at the step edge by the interface (see schematic configuration in Fig. 1b) and further relaxed. The Gibbs free energies of the reactions on the surfaces were calculated based on the following equations [39]:

$$\Delta G_1 = \Delta G_{HO^*} - \Delta G_{H_2O}(l) - eU + K_b T \ln a_{H^+} \quad (1)$$

$$\Delta G_2 = \Delta G_{O^*} - \Delta G_{HO^*} - eU + K_b T \ln a_{H^+} \quad (2)$$

$$\Delta G_3 = \Delta G_{HOO^*} - \Delta G_{O^*} - eU + K_b T \ln a_{H^+} \quad (3)$$

$$\Delta G_4 = \Delta G_{O_2} - \Delta G_{HOO^*} - eU + K_b T \ln a_{H^+} \quad (4)$$

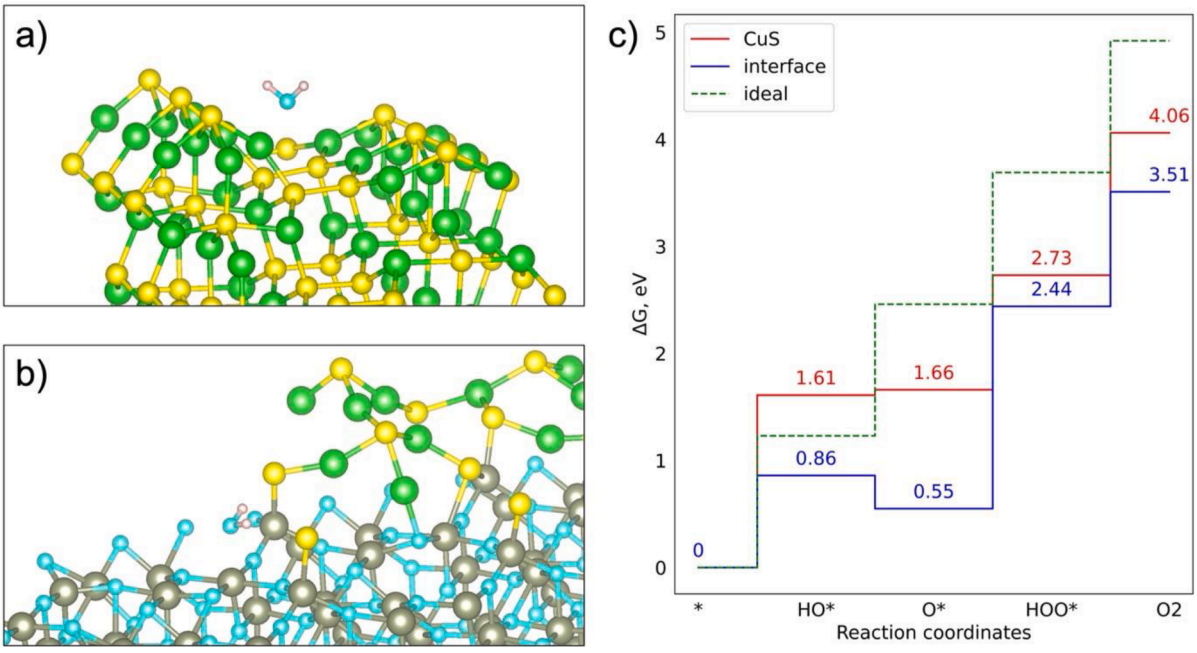

Fig. 1. Initial atomic configuration and the position of the adsorbing species on a) a CuS surface and b) the step edge close to the Cr_2O_3/CuS interface. c) Change of the Gibbs free energy during the OER process on the surface of CuS and at the interface of Cr_2O_3/CuS, compared to the ideal scenario.

The charge difference calculations were performed for the Cr_2O3/CuS interface system via the subtraction of separately calculated charges for the Cr_2O_3 and CuS layers. The analysis of the conducted calculations was done through Transition State Tools for VASP by Henkelman group [45].

2.2. Synthesis of CrOx on carbon fiber (CF)

Chemical vapor deposition (CVD) method was employed to synthesize the CrOx platform. Prior to the growth, the CF substrate was immersed into a (1:1:1) mixture of acetone, ethanol, and deionized water for ultrasonic cleaning. Then, 0.5 g of Cr_2O_3 powder was placed at the center of CVD tube and the cleaned CF was kept downstream by cm 8–12 cm away from the center. The chamber pressure was pumped down to about 0.1 Pa. Before increasing the temperature, the tube was flushed with Ar gas three times to ensure the Ar-saturated growth chamber. With this condition, the temperature was raised to 450 °C within 30 min from room temperature, and dwell at that temperature for 1hr with a constant flow of Ar (50 sccm). After the synthesis process, the CVD machine was allowed to cool to room temperature. The product, CrOx grown on CF, was taken for the next step to grow the heterostructure.

2.3. Synthesis of CrOx-CuS on CF

For the hydrothermal step, 0.2 mmol of $Cu(NO_3)_2{\cdot}6H_2O$ and 2 mmol of thiourea were dissolved in 80 mL of distilled water. This content was then transferred into Teflon-lined stainless steel autoclave reactor containing the CrOx/CF product obtained in the fist step above. The autoclave reactor was locked properly and placed in a pre-heated oven at 120 °C for 12 h. Eventually, the autoclave was cooled down to room temperature, and the product, CrOx-CuS/CF, was taken out for characterizations and electrochemical measurements.

2.4. Characterization

Field-emission scanning electron microscopy (FESEM), Magellan XHR 400L with a 10 KV electron beam was used to investigate the morphology of the as-synthesized samples. Further detail on the morphology, crystal structure and composition were obtained from FEI Tecnai F20 highresolution transmission electron microscope (HRTEM), equipped with a Schottky emitter operating at 200 kV. Elemental analysis was performed by energy-dispersive X-ray spectroscopy (EDS), coupled to scanning transmission electron microscopy (STEM-HAADF) to map elemental distribution. X-ray diffractogram was obtained from PanAnalytical Empyrean XRD using Cu kα radiation. High-resolution X-ray photoemission spectroscopy (XPS) spectra were acquired at the VUV-Photoemission beamline of the synchrotron Elettra (Trieste, Italy) with a Scienta R-4000 electron spectrometer and photon energy 750 eV. All samples were measured at room temperature.

X-ray absorption spectroscopy (XAS) measurement in fluorescence mode, was carried out at the XRF-IAEA experimental end station of of the synchrotron Elettra on CrOx/CF, CrOx-CuS and control samples (Cr foil, Cr3+, Cr6+) on Cr edge. The samples were mounted on a Teflon sample holder using Kapton tape in an ultra-high vacuum chamber (operated at 2×10^{-7} mbar). A Si (1 1 1) double crystal monochromator of 1.4×10^{-4} resolving power and a higher-order suppressor (HOS) were used to monochromatize the incoming radiation from the bending magnet source of the Elettra ring and to ensure the spectral purity, respectively. A diamond beam monitor was used to monitor the incident beam intensity from the monochromator. Before XAS measurements, incident X-ray energies emitted from the beamline were calibrated by performing absorption edge measurements of a pure Cr metal foil. The sample was placed at 45° with respect to the incident beam. A silicon drift detector (SDD, Bruker Nano GmbH, XFlash 5030, 131 eV energy resolution at Mn-Ka) with a 30 mm^2 active area, equipped with an ultra-thin polymer window (Moxtek AP3.3, 50 mm^2 nominal active area and 0.38 mm thickness) was used to collect the emitted fluorescence radiation. The sample to detector distance was optimized to 15 mm in respect to the detector dead time, acquisition time at each energy and XAS spectra with satisfactory good statistics for a collimated incident beam size of 500 × 500 μm^2. The raw data were processed using the standard procedures for XAFS data treatment including pre-edge background subtraction, post-edge bare ion model definition, and edge jump normalization.

2.5. Electrochemical measurements

H-type three-electrode cell configuration connected to an electrochemical workstation ModuLab XM ECS potentiostat (Solartron Instrument) was used to perform electrochemical testes in 1MKOH electrolyte. The cell was continuously purged with high-purity Ar gas for 30 min prior to each measurement. A graphite rod, saturated calomel electrode (SCE), and the synthesized samples were used as the counter, reference, and working electrodes respectively. The OER performance was evaluated by measuring the anodic linear sweep voltammetry with a sweep rate of 5 mV s^{-1}. All of the potentials are automatically iR-corrected and presented with respect to the reversible hydrogen electrode (RHE). The durability test was carried out through chronopotentiometry run at a current densities of 10 mA/cm^2, 30 mA/cm^2, 100 mA/cm^2. Electrochemical impedance spectra (EIS) measurements were carried out from 0.1 to 100 000 Hz with an amplitude of 5 mV and an overpotential of 0.3 V. The electrochemical double-layer capacitance, which is expected to be linearly proportional to the ECSA, was determined by measuring the capacitive current at non-Faradic region from scan rate dependent CV runs.

3. Results and discussions

3.1. Theorethical insights

When two dissimilar materials are brought into contact, the crystal structure/electronic structure near interface region are different from the either sides. Before conducting the experiment, computational models were first designed to understand these intriguing features of the interface between CuS and Cr_2O_3. To this end, density functional theory (DFT) calculations were performed to investigate the OER performance of the CuS slab and the influence of a Cr_2O_3 sublayer on the Cr_2O_3/CuS joint system on the OER process. The corresponding free energy changes resulting from the OER on a CuS surface and close to a step edge of a Cr_2O_3/CuS interface are shown in Fig. 1. The procedure of the ΔG_{1-4} calculation is thoroughly described in previous work [46]. In short, the calculations were done using the computational standard hydrogen electrode, using the initial atomic configurations for the two systems as shown in Fig. 1a and b. The results are compared with the ideal scenario in which the change in the Gibbs free energy for each reaction step requires 1.23 eV. As seen in Fig. 1c, the Cr_2O_3/CuS could attain lower energy levels than bare CuS. For the CuS, the energy limiting step is for the HO* coordinate, meaning that the OER process cannot start at the overpotential of 1.23 eV and simply requires the application of a higher external potential, *eU*. However, once the required overpotential is provided, the OER will be conducted below the zero-limit line.

For the interface configuration, Fig. 1b, it is obvious that the first two steps require less overpotential to start the OER, however, the energy limiting value is determined by the third step, being higher than for CuS. Nevertheless, a closer look at the adsorption of OOH* on the Cr_2O_3/CuS interface shows that the molecule spontaneously decomposes, which results in lower values of the total energy of the system, contributing to the values of ΔG_3 and ΔG_4. Such behavior indicates that the decomposition of the molecules at these steps should require less energy than shown on the graphs, indicating less energy-requiring OER flow.

The distribution of the charge density difference at the interface

(Fig. S1b) further supports this conclusion. It appears that the charges are mainly distributed between the CuS layer and the Cr_2O_3 layer directly below. It is more favorable for the unstable HOO* to break and create bonding states with Cr and S (Fig. S1c), hence lowering the total energy of the system. The oxygen atoms are attached to the positively charged part of the surface, whereas the hydrogen atom stays close to the negatively charged part. According to the acquired results, which display lower overpotential and spontaneous decomposition of the HOO* molecule, it was estimated that the OER at the interface of the Cr_2O_3/CuS slab should be more efficient compared to the CuS surface. The finding from computational perspectives points out that the interface between CuS and Cr_2O_3 provides a convenient platform for optimum adsorption/desorption of intermediates in OER process. Inspired by the outcomes of the computational studies, we designed experimental routes to realize the formation of heterojunction between the two components.

3.2. Characterizations for morphology, crystal structure and composition

The method employed to synthesize the desired heterostructure is schematically depicted in Fig. 2.The CrOx platform was first grown on CF substrate *via* a CVD method from the bulk Cr_2O_3 powder. This product was then introduced to the hydrothermal reactor where the growth of CuS nanosheets took place on the already grown CrOx/CF nanosheets, thus yielding CrOx-CuS/CF heterostructure. The morphology of the as-synthesized product was examined though field emission scanning electron microscopy (FE-SEM). Fig. 3a shows the hexagonal nanosheet with distinguished edges for CrOx-CuS material. The High-angle annular dark-field scanning transmission electron microscopy (HAADF – STEM) image in Fig. 3b (also Fig. S3a) is even more clear to depict the presence of composites in the final product, thanks to the differences in contrast that emerge from the different chemical composition. It is apparent that, the flakes of different components superimposed on top of one another, representing CuS flakes on the top of CrOx ones. The morphology of the bare CrOx (i.e the CVD product) is depicted in Fig. S2 showing a fairly resembling to the heterostructure, except for the absence of a rougher surface. The HAADF-STEM was also employed to analyze the element distribution (red square in Fig. 3b). The resulting EDS mapping images reveal that the material contains Cr, Cu, S, and O elements with uniform distribution wherein the pattern of Cr aligns with O, and that of Cu with S. The crystal structure of the as-synthesized material was examined through high-resolution TEM (HRTEM) and X-ray diffraction (XRD) patterns. Fig. 3d and e show the HRTEM images revealing the existence of Cr_2O_3 and CuS (enlarged images are depicted in Fig. S4 for clarity). The spatial frequencies of the crystallite displayed in the FFT are compatible with covellite ($d_{spacing}$ = 3.3 Å) corresponding to the (1 0 0) crystal planes. This suggests that the CuS is present. Moreover, it's possible to notice that the sample shows a pronounced local contrast variation, that can be attributed to a poly-crystalline system. Selected Area Electron Diffraction (SAED) pattern obtained by centering the aperture on the area highlighted in the HRTEM image further affirms a poly-crystalline pattern with the typical d-spacings of Covellite phase (CuS). By placing the focus of the analysis on the lower contrast phase it was possible to elucidate another crystalline character. Accordingly, the FFT displaying d spacings of 1.8 Å, 2.1 Å, and 3.6 Å are suggestive of the crystal planes (0 2 4), (1 1 3), (0 1 2) respectively in eskolaite Cr_2O_3. Further solidification of the findings was sought from XRD. Fig. 3f displays the XRD patterns of the CrOx-CuS composites in which all the diffraction peaks can be indexed to Cr_2O_3 (PDF#38-1479), CuS (06-0464) and the CF substrate indicating the successful growth of heterostructure mainly composed of Cr_2O_3 and CuS on CF. The XRD pattern of the bare CrOx sample is provided in Fig. S2c to elucidate the advent of new peaks in the heterostructure and diminishing of those meant for Cr_2O_3 (as compared to the single component one) following the growth of CuS. These results suggest that the successful growth of CuS on CrOx platform that would deliver a conducive interface for enhanced OER activity. Another compelling phenomenon is the nature of electron transfer between these two components as it is crucial to probe the mechanism behind the catalytic activities.

We employed XPS to get insight into the near-surface electronic structure of the catalysts. Given that the XPS analysis is surface sensitive, it only sees the depth of few nanometers. For this reason, we expect different results from the bulk sensitive XRD. Accordingly the metal components (Cr and Cu) appear in different forms on the surface of the material. The surveys in Fig. S5 can be used to follow the changes of the catalysts at various stages of the experiment. Fig. 4a shows the XPS spectrum of Cr 2p in pristine CrOx where broad Cr2p3/2 and Cr2p1/2 features are observed at about 577 and 587 eV. The deconvolution of the spectrum gives four Cr2p3/2 peaks at 575.67 eV, 576.77 eV, 577.97 eV, 581.07 eV that can be associated to Cr in CrO_2, Cr_2O_3, CrO(OH)/ $Cr(OH)_3$, and CrO_3 [47,48]. The presence of multiple oxidation states can further assist strong electron interactions within the transition metal compounds, thereby enhancing the catalysis toward OER [49]. This result is in agreement with other reports [25,50]. The peak pertaining to metallic chromium (~574.3 eV) is not observed. The O1s XPS spectrum of pristine CrOx (Fig. 4b) shows peaks at binding energies of 529.94 eV and 531.24 eV, assigned to lattice oxygen ($Cr(OH)_3$ and Cr_2O_3, respectively [51]), and a peak at 532.44 eV, which is assigned to surface defects and/or adsorbed surface hydroxyls. The core level analysis of the CrOx-CuS heterostructure is presented in Fig. 4c–f. Owing to the electron transfer between CrOx and CuS, there is a shift (~0.4 ÷ 0.6 eV) in the binding energies of the Cr2p peaks (Fig. 4c). The signal is strongly attenuated with respect to the pristine system due to the presence of the CuS coating. It is also noteworthy that the Cr^{6+} peak diminishes in the

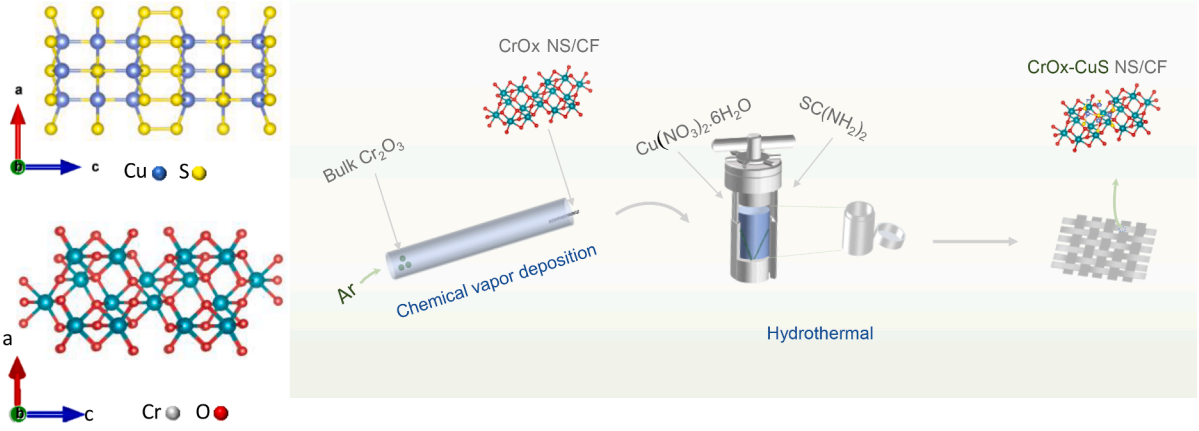

Fig. 2. Schematics depicting the molecular models of detected crystals and synthesis of CrOx-CuS heterojunction.

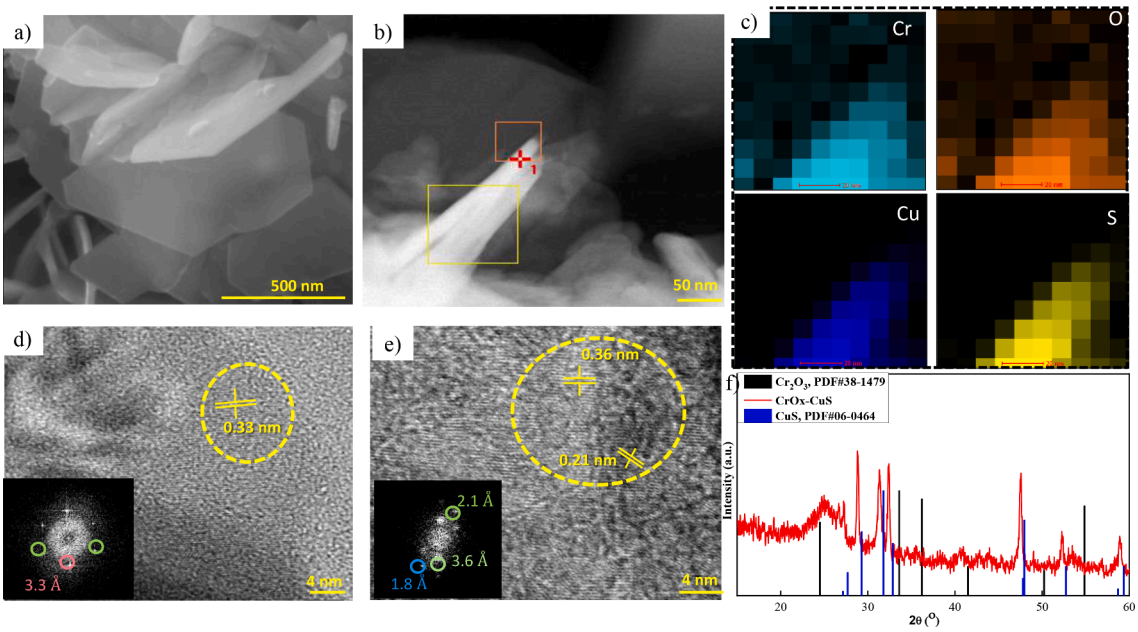

Fig. 3. Morphology, crystal structure and elemental distribution of CrOx-CuS nanosheets on CF. (a) SEM image. (b) STEM image. (c) EDS mapping. (d, e) HRTEM images with inset illustrating the spatial frequencies of the crystallite displayed in the FFT. (f) XRD pattern.

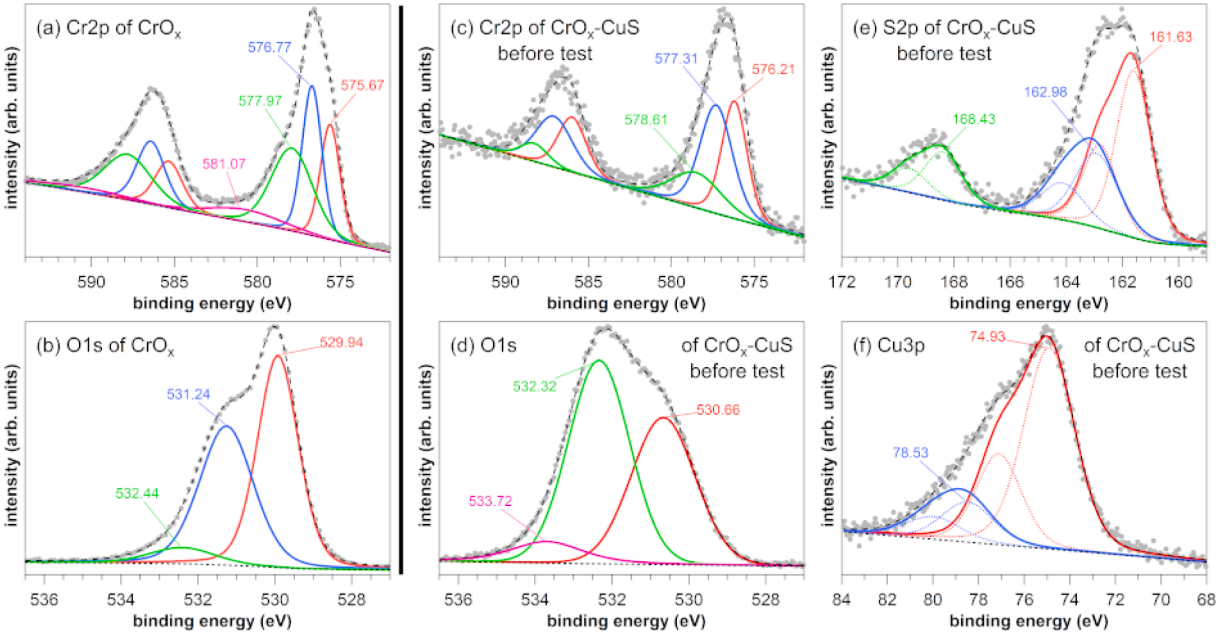

Fig. 4. High-resolution XPS spectra of CrOx (a,b) and CrOx-CuS before the catalytic test (c–f).

case of CrOx-CuS, corroborating the electronic perturbance at the interface as a result of charge transfer across the interface. In the O1s spectrum of Fig. 4d, the $Cr(OH)_3$ and Cr_2O_3 components give rise to a single peak at 530.66 eV. The peak at 532.32 eV can be attributed to the overlap of OH/defects and $CuSO_4$ emission. The peak at 533.72 eV is ascribed to adsorbed water. The S2p spectrum in Fig. 4e displays three components with $S2p_{3/2}$ peaks at 161.63, 162.98 and 168.43, corresponding to CuS (S^{2-}), CuS_2 (S_2^{2-}) and $-SO_4^{-2}$ [52,53]. The spectrum in Fig. 4f reveals $Cu3p_{3/2}$ peaks at binding energies of 74.93 eV and 78.53 eV corresponding to covellite and to Cu nearby by $-SO_4^{-2}$ [52].

To further elucidate the oxidation state and geometry of an element, we characterized the pure CrOx and the heterostructure CrOx-CuS with X-ray absorption spectroscopy (XAS). We have also measured commercial samples for ease of commenting, *via* comparison, on the plausible nature of the metal in our samples. Fig. 5a shows the X-ray absorption near edge structure (XANES) of Cr K edges in various samples. It is reported [53–57] that the pre-edge feature offers a crucial information and has been shown to be an electronic transition within samples containing elements with highly changeable oxidation states. As confirmed from our XPS analysis, Cr appears in multiple oxidation states which change when the heterostructure is formed as compared to the single component CrOx sample. The XANES profiles are depicted in Fig. 5a. The pre-edge feature for Cr^{6+} appears at around 5998 eV which represents the transition of electron from 1s to 3d orbital. This transition is allowed in tetrahedral compounds, lacking an inversion center, and hence the intense pre-edge peak is apparent for materials containing

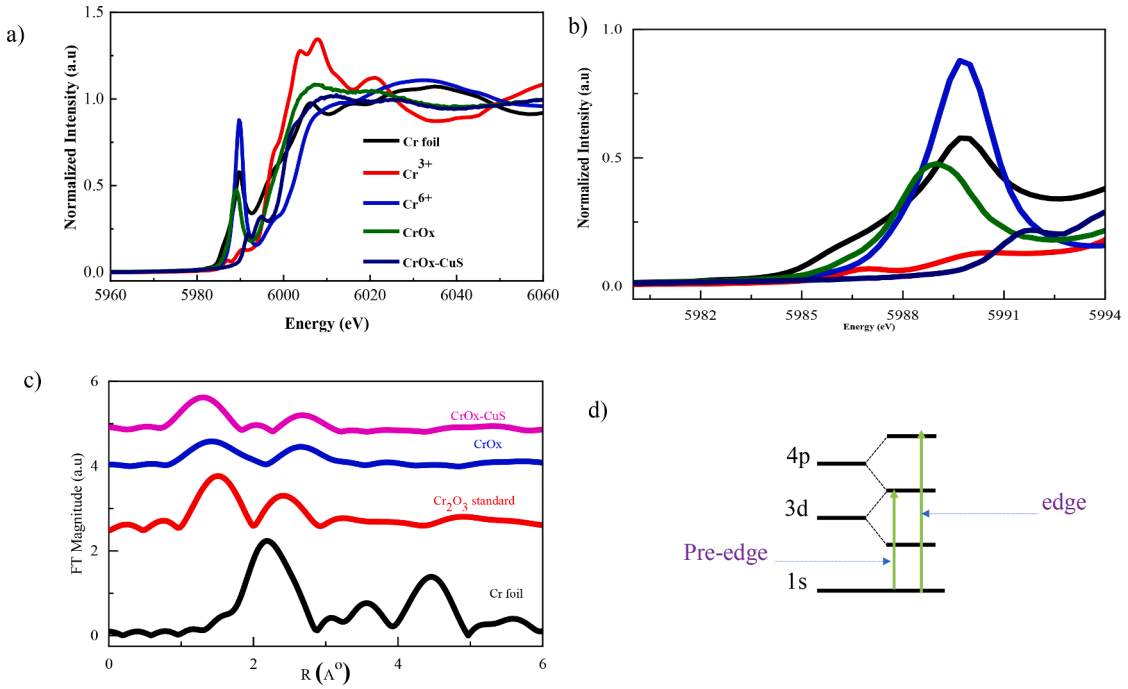

Fig. 5. Structure analysis of CrOx-CuS by X-ray absorption fine structure (XAFS). (a) X-ray absorption near edge spectra (XANES) of CrOx-CuS for Cr K-edge. (b) Enlarged pre-edge figure for Cr K-edge. (c) Fourier transformed (FT) k3-weighted χ(k)-function of the EXAFS spectra for a Cr K-edge. (d) Diagram depicting electron transition associated to pre-edge and main peaks.

Cr^{6+} components [57]. On the other hand, the (1s → 3d) electron transition in octahedral Cr^{3+} components is a forbidden transition. This geometry represents where Cr is located at the crystal site with the center of inversion. Therefore, relatively low intensity of the pre-edge peak is expected for materials with octahedral configuration [57]. Based on these premises, the inset of Fig. 5b illustrates a considerable pre-edge feature of Cr in CrOx sample. Apparently, this feature significantly weakens for the case of CrOx-CuS sample. This highlights the diminishing tetrahedral state in the heterostructure as a result of electron transfer between CrOx and CuS, which agrees well with our XPS finding. The main edge peak represents the transition the 1s → 4p electron transition (Fig. 5d). Accordingly, the absorption energy of Cr-K edge in both CrOx and CrOx-CuS is higher than that of commercial Cr metal and Cr^{3+} standards but lower than that of commercial Cr^{6+} sample. From this observation, it can be deduced that the plausible oxidation state of Cr in the heterostructure is above 3+ and below 6+. In order to have depth insight into the structural change after CuS growth, we performed Fourier transform (FT) EXAFS analysis at Cr K-edge (Fig. 5c) for CrOx, CrOx-CuS and the control samples (with Cr^0 and Cr^{3+}). It is worth noting that the peak position of Cr-Cr bond in CrOx-CuS (d_{Cr-Cr} = 2.86) is slightly larger than that in CrOx (d_{Cr-Cr} = 2.89). This can be attributed to the formation of larger Cr-Cu kind bond in addition to the Cr-Cr bond. Such localized structure perturbation after CuS growth is considered as the origin of unsaturated sites/defects and thereby further triggering the electrocatalytic activity. Interestingly, the fitted Cr K-edge EXAFS results show the reduced coordination number of Cr-Cr in the case of CrOx-CuS (2.48 ± 0.24) as compared to the CrOx sample (2.88 ± 0.39). This can be related to the induced vacancies around the Cr metal, that are acknowledged to boost catalysis in various applications [58,59]. Similarly, the cordination number of Cr-O for CrOx-CuS (2.75 ± 0.56) which is much lower than that Cr-O for CrOx of (2.86 ± 0.42). This means the creation of a large number of O-defect sites. The obtained defective structure with a low coordination environment in CrOx-CuS would improve the electronic conductivity and facilitate the adsorption process of OH– onto metal cations, thereby increasing the intrinsic catalytic activity. Detailed fitting results for Cr centers, further corroborating the above conclusion, are presented in Fig. S6 and Tables S1.

3.3. Electro-catalytic performances

To understand how the interface and the defects/low-coordinated central metal atom affect the OER catalytic performance, the prepared materials were directly evaluated in 1 M KOH solution. The alkaline electrochemical performance toward OER was evaluated in a three electrode system where the synthesized samples (CrOx/CF, CrOx-CuS/CF), saturated calomel, and graphite rode were employed as working, reference and counter electrodes respectively. The catalytic activities were then assessed by linear sweep voltammetry. As shown in Fig. 6a, there is no remarkable activity observed in the case of the bare CF substrate, substantiating the fact that the catalytic activity is due to the grown materials. The heterostructure, benefitting from the active interface, exhibits lower overpotential (190 mV vs RHE,) at 10 mA cm^{-2}; with an improvement of 200 mV as compared to CrOx. Further corroboration can be seen from the Tafel plot in Fig. 6b extracted from the polarization curve in Fig. 6a. The smaller Tafel slope (57 mv dec^{-1}) recorded for CrOx-CuS reveals the fast kinetics taking place during OER process. The formation of heterostructure is associated with the abundant exposure of active sites as a result of the new interface formation between dissimilar materials. Therefore, it is crucial to understand the electrochemical active area of catalysts for OER which can be estimated by the double-layer capacitance (C_{dl}) around the electrode surface. To unveil this, we calculated the C_{dl} by monitoring the current density in the non-Faradic region with different scan rates [60]. The Cvs run for obtaining these data are presented in Fig. S7. Fig. 6c depicts a higher value of C_{dl} for the case of CrOx-CuS. The large electrochemical double-layer capacitance indicates the exposure of the highest active sites, which is believed to be one of the possible reasons for the enhanced OER activity. The high catalytic activity of CrOx-CuS was further evidenced by analyzing the electronic impedance spectroscopy (EIS). The Nyquist plots at η = 300 mV in Fig. 6d display typical semicircles for the catalysts. Following a relevant equivalent circuit (inset), the fitted results

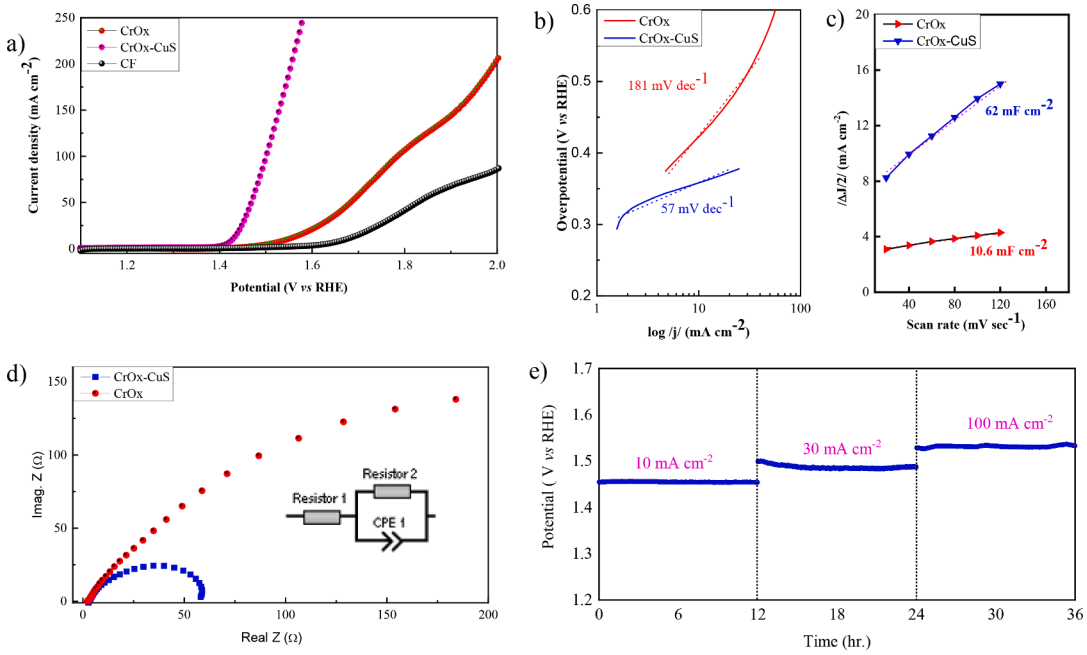

Fig. 6. Electrocatalytic activity performance for catalyzing water oxidation. (a) Linear sweep voltammetry (LSV) curves, scan rate: 5 mV s^{-1}. (b) Tafel plots extracted from LSV curves. (c) Double-layer capacitance (Cdl) measurements of CrOx-CuS and CrOx catalysts. (d) Comparison of Nyquist plots for the CrOx-CuS vs CrOx samples. (e) Chronopotentiometric tests of the CrOx-CuS catalyst at a constant current densities of 10 mA/cm^2, 30 mA/cm^2, and 100 mA/cm^2.

indicate the smaller Rct (64 Ω) of CrOx-CuS as compared to the CrOx sample (455 Ω). Details of the fitting parameters are given in the supporting information (Fig. S8). This highlights that the formation of heterointerface between CrOx and CuS triggered efficient electron transfer and fast ion diffusion, thereby yielding accelerated O_2 gas evolution. To evaluate electrochemical stability, long-term test was conducted using chrono-potentiometry measurement at 10 mA cm^{-2}, 30 mA cm^{-2}, and 100 mA cm^{-2} (Fig. 6e). It is noteworthy that the overpotential shows only negligible change for over 36hr of test, suggesting superior stability of the catalysts. The recorded perofmance in this work fairly compares to the recently reported materials in the litrature (TableS2).

3.4. Post-catalytic studies

It is evident that the surface of phosphides, chalcogenides, etc undergo some sort of surface reconstruction before the commencement of OER catalysis. The transformed surface is more conductive and it is the one that acts as the true catalyst [61]. We have experimentally demonstrated this for the case of phosphides in our previous study [62].

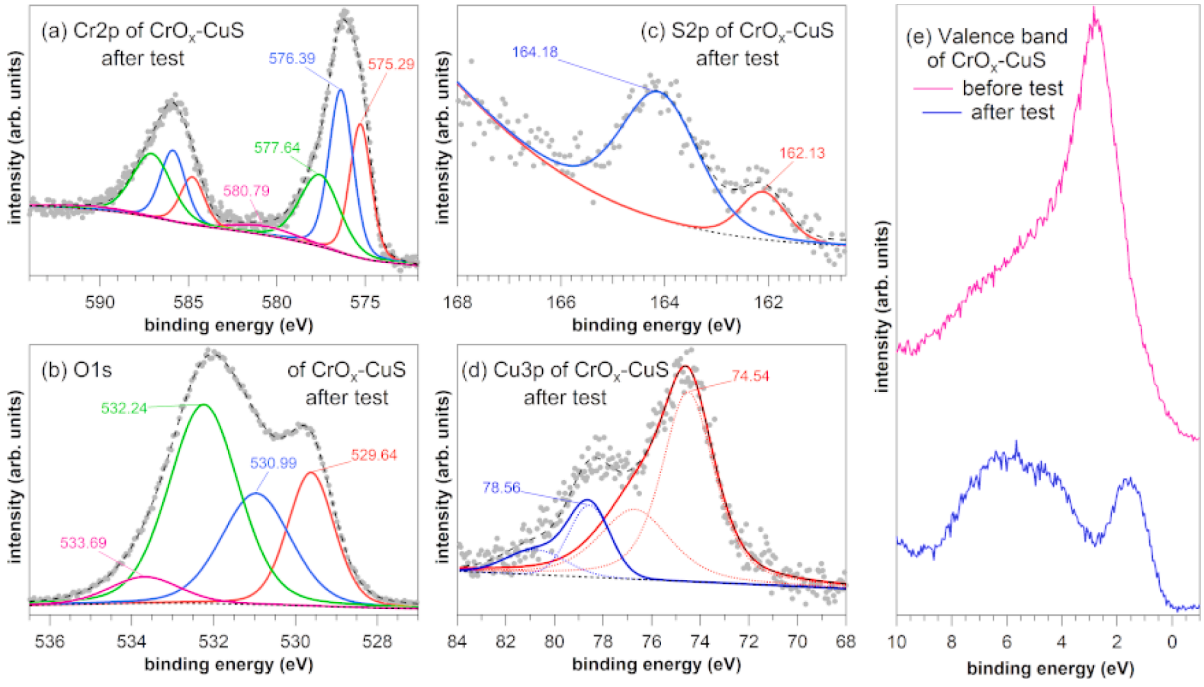

Fig. 7. Post-catalytic test characterization of CrOx-CuS by XPS (a–d). Comparison of the valence band XPS spectra of CrOx-CuS before and after the test (e).

The potential reasons for such enhancement could be: i) The derived metal oxides/hydroxides increases the electrochemically active surface area, inducing the improvement of the OER activity. ii) The metal chalcogenides are more conductive than the corresponding metal oxides/hydroxides and thus could serve as the conductive scaffolds for the derived metal oxide/hydroxide species. iii) There are synergistic electronic interactions between the different components that make the composite electro catalysts better than the intrinsic oxides [63]. Here, XPS characterization of the CrOx-CuS catalyst after OER reaction was also carried out to ascertain whether there was a possibility of component and structural evolution during the OER process of the prepared catalyst. It is evident from Fig. S5 that all the elemental components are still present after the test, except for the partly leaching of Cu and S on the surface. We have also witnessed a significant amount of K (from the electrolyte, 1 M KOH) after the OER test. Fig. 7 reports details of the core level analysis. In both Cr 2p and Cu 3p spectra (Fig. 7a and b), the peaks meant for metal sulfate/hydroxide at BE of 578.71 eV (Cr—S—O) and 78.41 eV (Cu-OH) are more pronounced after catalysis of OER. The same observation can be made from the O_{1s} XPS spectra (Fig. 7c). The XPS spectra of S2p after the OER test shows that there is a significant decrement in the content of sulfur on the surface of the catalyst. Yet, we can infer that there are still peaks at binding energies of 162.3 eV and 164.2 meant for the presence of a small amount of metal sulfur bonds at the surface (Fig. 7d). Notably, transition metal sulfides are very promising catalysts for water splitting. Especially in OER, the surface reconstructed metal-sulfates greatly contribute to electrical conductivity and activity [64]. Our post-OER XPS analysis uncovers higher binding energy S species corroborating the formation of oxysulfides. These results suggest that the surface may turn into metal oxyhydroxide/sulfate, which is supposed to host the true catalysis. Such induced species are believed to be more conductive (since they are in the vicinity of a more conductive chalcogenide) [65]. To get more insight into the surface reconstruction during OER, we compared the valence band spectra before and after OER activity (Fig. 7e). Before the OER test, a peak centered at about 2.5 eV represents the signature of the 3d level of Cu with contribution from O and C levels at higher energies [66]. After OER, the appearance of a Cr 3d peak is evident at about 1.5 eV, while the Cu-related is strongly suppressed. These results are in agreement with the core level analysis, suggesting the leaching (and hence the advent of unsaturated/active sites) around the Cr sites along with the reduced amount of Cu upon the electrochemical process. Further solidification on the elemental leaching can be sought from the bond disorder across the heterojunction. A larger Debye–Waller factor was observed for CrOx-CuS (Table S1), indicating the presence of structural distortion around the Cr centers as a result of the metal vacancy formation.

4. Conclusion

Heterojunction containing CrOx and CuS have been fabricated through subsequent CVD and hydrothermal method. The characterization results confirmed the co-existence of both phases with multiple oxidation states of the metals demonstrating reduced coordination number. We found that the formation of heterointerface gave rise to the advent of defects, unsaturated sites that are responsible for dramatically enhanced electrocatalytic OER activity. This finding was inspired by first-principles calculations. The post-OER characterization revealed the surface reconstruction into the corresponding oxyhydroxide/sulfate with improved conductivity as compared to the one before catalysis. Meanwhile, the good conductivity of the electrochemically induced phase contributes to the high-efficiency electron transport between electrode and reactive sites. This type of interface comprising of compounds with promising track record in their single component form could revolutionize the catalytic paradigm, showing great promise for the rational design of advanced catalysts for various electrochemical reactions.

Declaration of Competing Interest

The authors declare that they have no known competing financial interests or personal relationships that could have appeared to influence the work reported in this paper.

Data availability

Data will be made available on request.

Acknowledgements

This work was supported by the Kempe Foundation (JCK1505, JCK1703, SMK1839), the Knut och Alice Wallenberg Foundation (grant number KAW 2016.346 and KAW 2020.0033), the Göran Gustafsson foundation, and the ÅFORSK Foundation. We would also like to thank HPC2N (Tetralith) for the allocation of high-performance computing time and resources through the Swedish National Infrastructure for Computing (SNIC). This work has been carried out within the agreement "Convenzione operativa per collaborazione scientifica tra CNR ISM e Dipartimento di Scienze Molecolari e Nanosistemi Università Cà Foscari Venezia (Prot.n. 709, 14/04/2021)". Partial support through the project EUROFEL-ROADMAP ESFRI is gratefully acknowledged." The authors would also like to acknowledge Dr. Giuliana Aquilanti and Dr. Gangadhar for their support during the synchrotron measurement of X-ray absorption fine structure at Elettra.

Appendix A. Supplementary data

Supplementary data to this article can be found online at https://doi.org/10.1016/j.cej.2022.139781.

References

[1] C.C.L. McCrory, S. Jung, J.C. Peters, T.F. Jaramillo, Benchmarking Heterogeneous Electrocatalysts for the Oxygen Evolution Reaction, J. Am. Chem. Soc. 135 (2013) 16977.
[2] L. An, Z. Zhang, J. Feng, F. Lv, Y. Li, R. Wang, M. Lu, R.B. Gupta, P. Xi, S. Zhang, Heterostructure-Promoted Oxygen Electrocatalysis Enables Rechargeable Zinc-Air Battery with Neutral Aqueous Electrolyte, J. Am. Chem. Soc. 140 (2018) 17624–17631.
[3] L. Juan, L. Yang, L. Naiyun, H. Yuzhi, Z. Xing, H. Hui, L. Yeshayahu, L. Shuit-Tong, Z. Jun, K. Zhenhui, Metal-free efficient photocatalyst for stable visible water splitting via a two-electron pathway, Science (80-.). 347 (2015) 970–974.
[4] Y. Li, M. Gong, Y. Liang, J. Feng, J.-E. Kim, H. Wang, G. Hong, B. Zhang, H. Dai, Advanced zinc-air batteries based on high-performance hybrid electrocatalysts, Nat. Commun. 4 (2013) 1805.
[5] H. Wang, H.-W. Lee, Y. Deng, Z. Lu, P.-C. Hsu, Y. Liu, D. Lin, Y. Cui, Bifunctional non-noble metal oxide nanoparticle electrocatalysts through lithium-induced conversion for overall water splitting, Nat. Commun. (2015).
[6] R.Sun, W. Guo, X. Han, X. Hong, Two-dimensional Noble Metal Nanomaterials for Electrocatalysis, Chem. Res. Chinese Universities. 36 (2020) 597.
[7] H. Wang, J. Qi, N. Yang, W. Cui, J. Wang, Q. Li, Q. Zhang, X. Yu, L. Gu, J. Li, R. Yu, K. Huang, S. Song, S. Feng, D. Wang, Dual-Defects Adjusted Crystal-Field Splitting of LaCo1−xNixO3−δ Hollow Multishelled Structures for Efficient Oxygen Evolution, Angew. Chem. Int.Ed. 59 (2020) (1961).
[8] A.A. Bushunov, M.K. Tarabrin, V.A. Lazarev, Review of Surface Modification Technologies for Mid-Infrared Antireflection Microstructures Fabrication, Laser Photon. Rev. 15 (2021) 2000202.
[9] B. Chen, L. Xu, Z. Xie, W.-Y. Wong, Supercapacitor electrodes based on metal-organic compounds from the first transition metal series, EcoMat. 3 (2021) e12106.
[10] J. Ji, Y. Bao, X. Liu, J. Zhang, M. Xing, Molybdenum-based heterogeneous catalysts for the control of environmental pollutants, EcoMat. 3 (2021) e12155.
[11] L. Li, Y. Zhang, Y. Zhou, W. Zheng, Y. Sun, G. Ma, Y. Zhao, Optical Fiber Optofluidic Bio-Chemical Sensors: A Review, Laser Photon. Rev. 15 (2021) 2000526.
[12] G. Zheng, W. Xiao, H. Wu, J. Wu, X. Liu, J. Qiu, Near-Unity and Zero-Thermal-Quenching Far-Red-Emitting Composite Ceramics via Pressureless Glass Crystallization, Laser Photon. Rev. 15 (2021) 2100060.
[13] Q. Zhang, D. Liu, P. Dang, H. Lian, G. Li, J. Lin, Two Selective Sites Control of Cr3+-Doped ABO4 Phosphors for Tuning Ultra-Broadband Near-Infrared Photoluminescence and Multi-Applications, Laser Photon. Rev. 16 (2022) 2100459.
[14] F. Calle-Vallejo, N.G. Inoglu, H.-Y. Su, J.I. Martínez, I.C. Man, M.T.M. Koper, J. R. Kitchin, J. Rossmeisl, Number of outer electrons as descriptor for adsorption processes on transition metals and their oxides, Chem. Sci. 4 (2013) 1245–1249.

[15] J. Suntivich, K.J. May, H.A. Gasteiger, J.B. Goodenough, Y. Shao-Horn, A Perovskite Oxide Optimized for Oxygen Evolution Catalysis from Molecular Orbital Principles, Science (80-.) 334 (2011) 1383.

[16] Y. Sun, H. Liao, J. Wang, B. Chen, S. Sun, S.J.H. Ong, S. Xi, C. Diao, Y. Du, J.-O. Wang, M.B.H. Breese, S. Li, H. Zhang, Z.J. Xu, Covalency competition dominates the water oxidation structure–activity relationship on spinel oxides, Nat. Catal. 3 (2020) 554–563.

[17] H. Li, S. Sun, S. Xi, Y. Chen, T. Wang, Y. Du, M. Sherburne, J.W. Ager, A.C. Fisher, Z.J. Xu, Metal-Oxygen Hybridization Determined Activity in Spinel-Based Oxygen Evolution Catalysts: A Case Study of ZnFe2–xCrxO4, Chem. Mater. 30 (2018) 6839–6848.

[18] L.J. Murray, M. Dinca, J. Yano, S. Chavan, S. Bordiga, C.M. Brown, J.R. Long, Highly-Selective and Reversible O2 Binding in Cr3(1,3,5-benzenetricarboxylate)2, J. Am. Chem. Soc. 132 (2010) 7856–7857.

[19] J. Baek, H. Jin Yun, D. Yun, Y. Choi, J. Yi, Preparation of Highly Dispersed Chromium Oxide Catalysts Supported on Mesoporous Silica for the Oxidative Dehydrogenation of Propane Using CO2: Insight into the Nature of Catalytically Active Chromium Sites, ACS Catal. 2 (2012) 1893–1903.

[20] D. Xu, M.B. Stevens, Y. Rui, G. DeLuca, S.W. Boettcher, E. Reichmanis, Y. Li, Q. Zhang, H. Wang, The role of Cr doping in NiFe oxide/(oxy)hydroxide electrocatalysts for oxygen evolution, Electrochim. Acta 265 (2018) 10–18.

[21] H. Park, E. Lee, M. Lei, H. Joo, S. Coh, B.P.T. Fokwa, Canonic-Like HER Activity of Cr1–xMoxB2 Solid Solution: Overpowering Pt/C at High Current Density, Adv. Mater. 32 (2020) 2000855.

[22] T. Murata, Y. Kozuka, M. Uchida, M. Kawasaki, Magnetic properties of spin frustrated spinel ZnFe2O4/ZnCr2O4 superlattices, J. Appl. Phys. 118 (2015), 193901.

[23] I. Persson, J. Halim, H. Lind, T.W. Hansen, J.B. Wagner, L.-Å. Näslund, V. Darakchieva, J. Palisaitis, J. Rosen, P.O.Å. Persson, 2D Transition Metal Carbides (MXenes) for Carbon Capture, Adv. Mater. 31 (2019) 1805472.

[24] Y. Lin, Z. Tian, L. Zhang, J. Ma, Z. Jiang, B.J. Deibert, R. Ge, L. Chen, Chromium-ruthenium oxide solid solution electrocatalyst for highly efficient oxygen evolution reaction in acidic media, Nat. Commun. 10 (2019) 162.

[25] M. Chandra, K. Bhunia, D. Pradhan, Controlled Synthesis of CuS/TiO2 Heterostructured Nanocomposites for Enhanced Photocatalytic Hydrogen Generation through Water Splitting, Inorg. Chem. 57 (2018) 4524–4533.

[26] G. Hou, Z. Cheng, L. Kang, X. Xu, F. Zhang, H. Yang, Controllable synthesis of CuS decorated TiO2 nanofibers for enhanced photocatalysis, CrystEngComm. 17 (2015) 5496–5501.

[27] L. Zhou, S. Dai, S. Xu, Y. She, Y. Li, S. Leveneur, Y. Qin, Piezoelectric effect synergistically enhances the performance of Ti32-oxo-cluster/BaTiO3/CuS p-n heterojunction photocatalytic degradation of pollutants, Appl. Catal. B Environ. 291 (2021), 120019.

[28] X. Xin, Y. Song, S. Guo, Y. Zhang, B. Wang, J. Yu, X. Li, In-situ growth of high-content 1T phase MoS2 confined in the CuS nanoframe for efficient photocatalytic hydrogen evolution, Appl. Catal. B Environ. 269 (2020), 118773.

[29] S. Conejeros, I. de P.R. Moreira, P. Alemany, E. Canadell, Nature of Holes, Oxidation States, and Hypervalency in Covellite (CuS), Inorg. Chem. 53 (2014) 12402–12406.

[30] A.Y. Bykov, A. Shukla, M. van Schilfgaarde, M.A. Green, A.V. Zayats, Ultrafast Carrier and Lattice Dynamics in Plasmonic Nanocrystalline Copper Sulfide Films, Laser Photon. Rev. 15 (2021) 2000346.

[31] K.B. Ibrahim, W.-N. Su, M.-C. Tsai, A.W. Kahsay, S.A. Chala, M.K. Birhanu, J.-F. Lee, B.J. Hwang, Heterostructured composite of NiFe-LDH nanosheets with Ti4O7 for oxygen evolution reaction, Mater. Today Chem. 24 (2022), 100824.

[32] T.A.T.A. Shifa, F. Wang, Y. Liu, J. He, Heterostructures Based on 2D Materials: A Versatile Platform for Efficient Catalysis, Adv. Mater. 1804828 (2018).

[33] T.A. Shifa, A. Vomiero, Confined Catalysis: Progress and Prospects in Energy Conversion, Adv. Energy Mater. 9 (2019) 1902307.

[34] P. Hou, D. Li, N. Yang, J. Wan, C. Zhang, X. Zhang, H. Jiang, Q. Zhang, L. Gu, D. Wang, Delicate Control on the Shell Structure of Hollow Spheres Enables Tunable Mass Transport in Water Splitting, Angew. Chem. Int. Ed. 60 (2021) 6926.

[35] P. Zhai, Y. Zhang, Y. Wu, J. Gao, B. Zhang, S. Cao, Y. Zhang, Z. Li, L. Sun, J. Hou, Engineering active sites on hierarchical transition bimetal oxides/sulfides heterostructure array enabling robust overall water splitting, Nat. Commun. 11 (2020) 5462.

[36] J. Joo, T. Kim, J. Lee, S.-I. Choi, K. Lee, Morphology-Controlled Metal Sulfides and Phosphides for Electrochemical Water Splitting, Adv. Mater. 31 (2019) 1806682.

[37] M. Zhu, J. Chen, L. Shen, M.E. Ford, J. Gao, J. Xu, I.E. Wachs, Y.-F. Han, Probing the surface of promoted CuO-Cr2O3-Fe2O3 catalysts during CO2 activation, Appl. Catal. B Environ. 271 (2020), 118943.

[38] C.-Y. Lee, T.-H. Jung, B.-H. Ha, Characteristics of CuO—Cr2O3/mordenite and its catalytic activity for combustion and NO decomposition, Appl. Catal. B Environ. 9 (1996) 77–91.

[39] Y. Zhang, Q. Li, H. Yuan, W. Yan, S. Chen, M. Qiu, B. Liao, L. Chen, X. Ouyang, X. Zhang, M. Ying, Mechanically Robust Irradiation, Atomic Oxygen, and Static-Durable CrOx/CuNi Coatings on Kapton Serving as Space Station Solar Cell Arrays, ACS Appl. Mater. Interfaces 14 (2022) 21461–21473.

[40] Q. Yan, P.T. Doan, H. Toghiani, A.C. Gujar, M.G. White, Synthesis Gas to Hydrocarbons over CuO-CoO-Cr2O3/H+-ZSM-5 Bifunctional Catalysts, J. Phys. Chem. C 112 (2008) 11847–11858.

[41] F. Severino, J. Laine, Effect of composition and pretreatments on the activity of copper-chromium-based catalysts for the oxidation of carbon monoxide, Ind. Eng. Chem. Prod. Res. Dev. 22 (1983) 396–401.

[42] G. Kresse, J. Hafner, Ab initio molecular-dynamics simulation of the liquid-metal–amorphous-semiconductor transition in germanium, Phys. Rev. B 49 (1994) 14251–14269.

[43] G. Kresse, D. Joubert, From ultrasoft pseudopotentials to the projector augmented-wave method, Phys. Rev. B 59 (1999) 1758–1775.

[44] J. Klimeš, D.R. Bowler, A. Michaelides, Van der Waals density functionals applied to solids, Phys. Rev. B 83 (2011), 195131.

[45] P. Xiao, D. Sheppard, J. Rogal, G. Henkelman, Solid-state dimer method for calculating solid-solid phase transitions, J. Chem. Phys. 140 (2014), 174104.

[46] I.C. Man, H.-Y. Su, F. Calle-Vallejo, H.A. Hansen, J.I. Martínez, N.G. Inoglu, J. Kitchin, T.F. Jaramillo, J.K. Nørskov, J. Rossmeisl, Universality in Oxygen Evolution Electrocatalysis on Oxide Surfaces, ChemCatChem. 3 (2011) 1159–1165.

[47] R. Cheng, B. Xu, C.N. Borca, A. Sokolov, C.-S. Yang, L. Yuan, S.-H. Liou, B. Doudin, P.A. Dowben, Characterization of the native Cr2O3 oxide surface of CrO2, Appl. Phys. Lett. 79 (2001) 3122–3124.

[48] M.C. Biesinger, C. Brown, J.R. Mycroft, R.D. Davidson, N.S. McIntyre, X-ray photoelectron spectroscopy studies of chromium compounds, Surf. Interface Anal. 36 (2004) 1550–1563.

[49] X. Liu, J. Wu, Coupling interface constructions of NiO–Cr2O3 heterostructures for efficient electrocatalytic oxygen evolution, Electrochim. Acta. 320 (2019), 134577.

[50] P.-L. Qin, H.-W. Lei, X.-L. Zheng, Q. Liu, H. Tao, G. Yang, W.-J. Ke, L.-B. Xiong, M.-C. Qin, X.-Z. Zhao, G.-J. Fang, Copper-Doped Chromium Oxide Hole-Transporting Layer for Perovskite Solar Cells: Interface Engineering and Performance Improvement, Adv. Mater. Interfaces 3 (2016) 1500799.

[51] N. Karikalan, R. Karthik, S.-M. Chen, C. Karuppiah, A. Elangovan, Sonochemical Synthesis of Sulfur Doped Reduced Graphene Oxide Supported CuS Nanoparticles for the Non-Enzymatic Glucose Sensor Applications, Sci. Rep. 7 (2017) 2494.

[52] R.A.D. Pattrick, J.F.W. Mosselmans, J.M. Charnock, K.E.R. England, G.R. Helz, C. D. Garner, D.J. Vaughan, The structure of amorphous copper sulfide precipitates: An X-ray absorption study, Geochim. Cosmochim. Acta. 61 (1997) 2023–2036.

[53] B.V. Crist, Handbooks of Monochromatic XPS Spectra: Volume 2: Commercially Pure Binary Oxides, XPS International LLC, 2004.

[54] I. Khalakhan, M. Vorokhta, X. Xie, L. Piliai, I. Matolínová, On the interpretation of X-ray photoelectron spectra of Pt-Cu bimetallic alloys, J. Electron. Spectros. Relat. Phenomena 246 (2021), 147027.

[55] F.E. Huggins, M. Najih, G.P. Huffman, Direct speciation of chromium in coal combustion by-products by X-ray absorption fine-structure spectroscopy, Fuel 78 (1999) 233–242.

[56] M.L. Peterson, G.E. Brown, G.A. Parks, C.L. Stein, Differential redox and sorption of Cr (III/VI) on natural silicate and oxide minerals: EXAFS and XANES results, Geochim. Cosmochim. Acta 61 (1997) 3399–3412.

[57] R.E. Shaffer, J.O. Cross, S.L. Rose-Pehrsson, W.T. Elam, Speciation of chromium in simulated soil samples using X-ray absorption spectroscopy and multivariate calibration, Anal. Chim. Acta 442 (2001) 295–304.

[58] Y. Dou, C.-T. He, L. Zhang, H. Yin, M. Al-Mamun, J. Ma, H. Zhao, Approaching the activity limit of CoSe2 for oxygen evolution via Fe doping and Co vacancy, Nat. Commun. 11 (2020) 1664.

[59] W. Li, D. Xiong, X. Gao, L. Liu, The oxygen evolution reaction enabled by transition metal phosphide and chalcogenide pre-catalysts with dynamic changes, Chem. Commun. 55 (2019) 8744–8763.

[60] Y. Wang, H. Arandiyan, K. Dastafkan, Y. Li, C. Zhao, Common Pitfalls of Reporting Electrocatalysts for Water Splitting, Chem. Res. Chinese Universities 36 (2020) 360.

[61] Tofik Ahmed Shifa, K. Yusupov, G. Solomon, A. Gradone, R. Mazzaro, E. Cattaruzza, A. Vomiero, In Situ-Generated Oxide in Sn-Doped Nickel Phosphide Enables Ultrafast Oxygen Evolution, ACS Catal. 11 (n.d.) 4520–4529.

[62] T.X. Nguyen, Y.-H. Su, C.-C. Lin, J.-M. Ting, Self-Reconstruction of Sulfate-Containing High Entropy Sulfide for Exceptionally High-Performance Oxygen Evolution Reaction Electrocatalyst, Adv. Funct. Mater. 31 (2021) 2106229.

[63] O. Mabayoje, A. Shoola, B.R. Wygant, C.B. Mullins, The Role of Anions in Metal Chalcogenide Oxygen Evolution Catalysis: Electrodeposited Thin Films of Nickel Sulfide as "Pre-catalysts", ACS Energy Lett. 1 (2016) 195–201.

[64] K. Liu, C. Zhang, Y. Sun, G. Zhang, X. Shen, F. Zou, H. Zhang, Z. Wu, E.C. Wegener, C.J. Taubert, J.T. Miller, Z. Peng, Y. Zhu, High-Performance Transition Metal Phosphide Alloy Catalyst for Oxygen Evolution Reaction, ACS Nano 12 (2017) 158–167.

[65] Q. Gao, W. Luo, X. Ma, Z. Ma, S. Li, F. Gou, W. Shen, Y. Jiang, R. He, M. Li, Electronic modulation and vacancy engineering of Ni9S8 to synergistically boost efficient water splitting: Active vacancy-metal pairs, Appl. Catal. B Environ. 310 (2022), 121356.

[66] G. Liu, T. Schulmeyer, J. Brötz, A. Klein, W. Jaegermann, Interface properties and band alignment of Cu2S/CdS thin film solar cells, Thin Solid Films 431–432 (2003) 477–482.